How to cite: Angew. Chem. Int. Ed. 2025, e202423562
doi.org/10.1002/anie.202423562

Organic Solar Cells

Isomerism Effect of 3D Dimeric Acceptors for Non-Halogenated Solvent-Processed Organic Solar Cells with 20 % Efficiency

Jia Wang, Peiran Wang, Tianqi Chen, Wenkai Zhao, Jiaying Wang, Baofa Lan, Wanying Feng, Hang Liu, Yongsheng Liu, Xiangjian Wan, Guankui Long, Bin Kan, and Yongsheng Chen**

Abstract: Organic photovoltaic materials that can be processed via non-halogenated solvents are crucial for the large-area manufacturing of organic solar cells (OSCs). However, the limited available of electron acceptors with adequate solubility and favorable molecular packing presents a challenge in achieving efficient non-halogenated solvent-processed OSCs. Herein, inspired by the three-dimensional dimeric acceptor CH8-4, we employed a molecular isomerization strategy to synthesize its isomers, CH8-4A and CH8-4B, by tuning the position of fluorine (F) atom in the central unit. The differing intramolecular fluorine-sulfur non-covalent interactions among these isomers led to differences in molecular pre-aggregation abilities (CH8-4B < CH8-4 < CH8-4A) in *o*-xylene (*o*-XY) solution, which significantly influence the film-forming process and the resultant morphological characteristics. Among these, the blend film of CH8-4, characterized by moderate molecular pre-aggregation, achieved optimal bi-continuous donor/acceptor phase separation. Consequently, the *o*-xylene processed PM6:CH8-4 device achieved a power conversion efficiency (PCE) of 18.1 %, outperforming that of two other devices. By incorporating L8-BO-D as a guest acceptor, we attained an impressive PCE of 20.0 % for the CH8-4-based ternary device, alongside a high PCE nearing 16 % for the mini-module (13.5 cm^2). Our findings underscore the potential of isomerism in 3D dimer acceptors to enhance the performance of eco-friendly OSCs.

[*] J. Wang,+ P. Wang,+ T. Chen, W. Zhao, J. Wang, B. Lan, G. Long, B. Kan
School of Materials Science and Engineering, National Institute for Advanced Materials, Nankai University, Tianjin, 300350, China
E-mail: kanbin04@nankai.edu.cn

W. Feng, H. Liu, Y. Liu, X. Wan, Y. Chen
State Key Laboratory and Institute of Elemento-Organic Chemistry, Frontiers Science Center for New Organic Matter, The Centre of Nanoscale Science and Technology and Key Laboratory of Functional Polymer Materials, Renewable Energy Conversion and Storage Center (RECAST), College of Chemistry, Nankai University, Tianjin, 300071, China
E-mail: yschen99@nankai.edu.cn

Introduction

Organic solar cells (OSCs) have attracted widespread attention due to their lightweight, semi-transparency, and intrinsic flexibility.[1,2] Advances in materials synthesis, interface engineering, and device optimization have allowed the power conversion efficiency (PCE) of small-molecular acceptors (SMAs) based OSCs to exceed 20 %,[3] indicating a great practical application potential of utilizing solar energy in the future. Moreover, the emergence of acceptor-donor-acceptor (A-D-A)-type SMAs provides an effective approach to balance the open-circuit voltage (V_{oc}) and short-circuit current density (J_{sc}) in the corresponding devices.[4] They possess several excellent properties, including well-defined molecular structures, excellent batch-to-batch reproducibility, and superior solution processability.[5] However, the SMAs are prone to exist in a thermally metastable state due to their self-aggregation characteristics, leading to detrimental effects on device stability.[6,7] Therefore, there is an urgent requirement to develop alternative acceptors with high photovoltaic performance and good stability.

Dimeric acceptors not only possess the desirable features of SMAs, such as well-defined molecular structures, excellent batch-to-batch reproducibility, and superior solution processability, but also exhibit excellent stability.[8–12] Currently, the most efficient OSCs often rely on halogenated solvents like chloroform and chlorobenzene, which pose risks to humans and the environment, and hence, are not adaptable to large-scale manufacturing.[13] Alternatively, toluene (Tol) and *o*-xylene (*o*-XY) are common non-halogenated solvents with high boiling points, providing extended processing window time during the film formation, which is importance for obtaining large-area and uniform blend films for module devices.[14,15] However, attaining equivalent efficiencies in OSCs processed with non-halogenated solvents is challenging, due to the scarcity of NFAs that possess adequate solubility, manageable pre-aggregation, and favorable crystallization kinetics in these solvents.[16] As presented in Table A1 of Appendix to the Supporting Information, with the advances in synthesis and optimization of device processes, some excellent oligomeric molecules on non-halogenated solvent systems have been reported in recent years.[17–21] For instance, Wei et al. synthesized a star-shaped giant trimer to fabricate organic solar cells by *o*-XY with over 19 % efficiency and a T_{90} of longer than 4,500 h

after continuous heating at 80 °C.[22] Sun et al. fabricated *o*-XY processed OSCs with 19.86 % efficiency by incorporating a trimeric guest acceptor (Tri-V) into the PM6:L8-BO-X host blend, which demonstrated exceptional photostability, retaining 80 % of its initial efficiency after 1380 h of continuous illumination.[23] These results indicate that the oligomeric acceptors would be the excellent candidates for fabricating high-performance and stable non-halogenated solvent-processed OSCs.[24]

Recently, based on the CH series with extended central-conjugation unit, we developed a new strategy to prepare three-dimensional (3D) dimeric acceptors with multiple A-D-A architectures (CH8-X series).[25] These 3D NFAs exhibit extremely low reorganization energy, fibrillar network film morphology and improved absorption coefficient in the near-infrared region, and better stability.[25] After blending with polymer donor PM6, satisfactory PCEs exceeding 17 % with low energy loss around 0.50 eV were achieved for the chloroform-processed or *o*-XY-processed binary OSCs.[26] Consequently, these results have motivated us to intensify our efforts towards the molecular innovation of these 3D dimeric acceptors, with the goal of developing high-efficiency, non-halogenated solvent-processed OSCs and mini-modules. Molecular isomerism is an effective strategy for molecular modification that significantly influences molecular structures, absorption, and energy levels.[27] Moreover, dimer acceptor isomers can have different self-assembly morphologies, which influence their distribution and arrangement within the active layer, resulting different device performance. As a typical example, Li et al. developed two vinyl π-spacer linking-site isomerized dimeric acceptors (EV-i and EV-o), and achieved a high PCE of 18.3 % for PM6: EV-i based OSCs with the o-XY as the solvent.[28] Despite this achievement, the isomerism strategies of dimeric acceptors have been less explored for non-halogenated solvent processed OSCs to date, particularly for the 3D dimeric acceptors. Therefore, a comprehensive understanding of the unique characteristics induced by molecular isomerism is imperative in terms of pre-aggregation, film formation kinetics, and micromorphology in non-halogenated solvents, for the future application of OSCs.

In this study, we designed and synthesized two isomerized 3D dimers of CH8-4, namely CH8-4A and CH8-4B, by leveraging the isomerization strategy of F on the central unit. Notably, the differing F–S interactions resulting from the various F sites lead to distinct pre-aggregation characteristics in these 3D dimeric acceptors.[29] Temperature-dependent UV/Vis absorption spectra analysis revealed that the degree of molecular pre-aggregation ability in *o*-XY solution increased in the order of CH8-4B to CH8-4 to CH8-4A. These unique properties significantly influence the film-forming process and the resultant morphological characteristics. Among these, the blend film of CH8-4, characterized by moderate molecular pre-aggregation, achieved optimal bi-continuous donor/acceptor phase separation with average fibril diameters of 13.9 nm. Consequently, enhanced charge transport and suppressed charge recombination resulted in a superior PCE of 18.1 % for the *o*-XY processed PM6:CH8-4 device, surpassing those of PM6:CH8-4A (16.7 %), and PM6:CH8-4B (17.8 %). Furthermore, the CH8-4 based ternary device exhibited a PCE of 20.0 %, along with a high V_{oc} of 0.906 V, J_{sc} of 27.70 mA cm^{-2}, and a fill factor (FF) of 79.6 %. These results surpassed those of most dimeric-acceptor-based devices processed with both halogenated and non-halogenated solvents (Figure S1).[30] Additionally, the corresponding module with an effective area of 13.5 cm^2, which consists of six sub-cells connected in series, exhibited an outstanding PCE approaching 16 %, showing the potential of these dimeric acceptors in fabricating large-area devices. This investigation has deepened our insight into the mechanisms of molecular isomerism and has developed a practically feasible strategy for correlating the performance of organic photovoltaics with molecular structures of 3D dimeric acceptors.

Results and Discussion

Figure 1a displays the chemical structures of CH8-4 along with its two isomers (CH8-4A and CH8-4B). Both new dimeric acceptors, CH8-4A and CH8-4B, were synthesized using the same methods as those described for CH8-4 in our previous work,[26] with the exception of utilizing 4-bromo-3-fluoro-1,2-benzenediamine intermediate for CH8-4A and 5-bromo-3-fluoro-1,2-benzenediamine intermediate for CH8-4B (see Scheme S1 and detail synthetic procedures in the Supporting Information). The energy levels of these dimeric molecules in the solid state were estimated via cyclic voltammetry (CV) to assess the influence of different F sites on energy levels (Figure S2). As illustrated in Figure 1b, the isomerization caused by the F atom positions has a slight effect on both the highest occupied molecular orbital (HOMO) and the lowest unoccupied molecular orbital (LUMO) energy levels. Concretely, the HOMO/LUMO values are measured to be −5.75/−3.79 eV for CH8-4, −5.72/−3.79 eV for CH8-4A, and −5.67/−3.78 eV for CH8-4B, respectively. Additionally, the differences in HOMO and LUMO energies between PM6 and CH8-4, CH8-4A, CH8-4B were within the range of 0.14–0.16 eV, which is sufficiently large to drive exciton dissociation in the corresponding blend films.[31]

Note that CH8-4, CH8-4A, and CH8-4B exhibit good solubility in *o*-XY due to their 3D structures and multiple long alkyl side chains. As shown in Figure S3a, we tested the UV/Vis absorption spectra of CH8-4, CH8-4A, and CH8-4B in *o*-XY solutions firstly. In their diluted solutions, all compounds exhibited strong absorption in the range of 450–850 nm, with maximum absorption peaks (λ_{sol}) located at 742, 740, and 739 nm for CH8-4, CH8-4A, and CH8-4B (Table S1), respectively. While, all of them exhibited distinct shoulder peak (0–0 peak) in the range of 780–830 nm in *o*-XY solutions, which may indicate the pre-aggregation properties of those 3D dimeric acceptors.[16,32,33] Therefore, we conducted temperature-dependent UV/Vis absorption spectra analysis of CH8-4, CH8-4A, and CH8-4B in *o*-XY solution in the ranges of 25–80 °C. As illustrated in Figure 1c–1e, all of them demonstrated temperature-dependent aggregation (TDA) behaviors in *o*-XY solutions. Specifi-

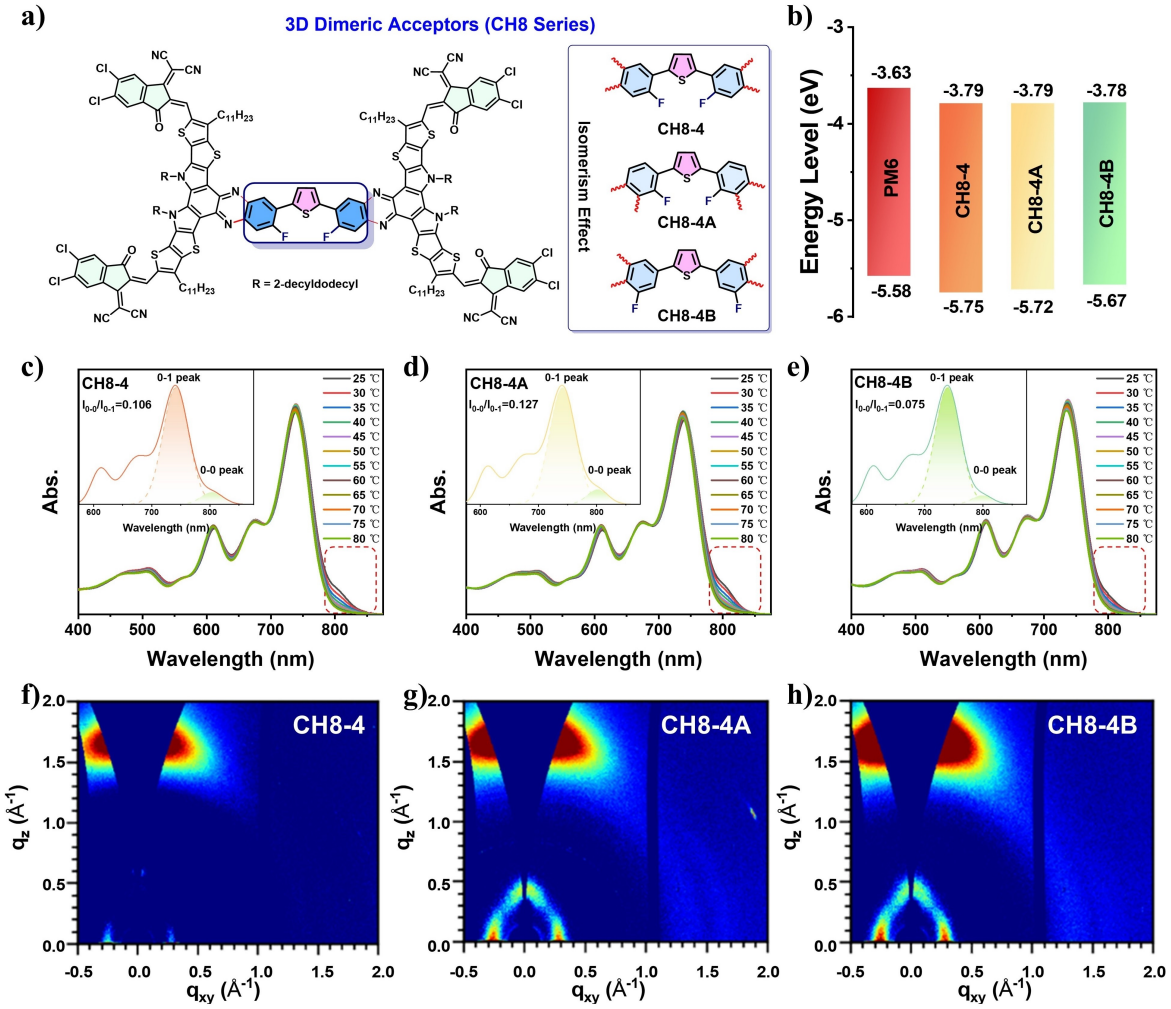

Figure 1. (a) The chemical structures of CH8-4, CH8-4A, and CH8-4B. (b) The energy levels of PM6, CH8-4, CH8-4A, and CH8-4B. (c-e) Temperature-dependent UV/Vis absorption spectra of CH8-4, CH8-4A, and CH8-4B in *o*-XY solution at 25 °C to 80 °C, respectively. Inset shows the peak-differentiation-imitating result of the corresponding absorption spectrum at 25 °C. (f-h) GIWAXS images of CH8-4, CH8-4A, and CH8-4B based neat films, respectively.

cally, as the temperature increased from 25 to 80 °C, the absorbance of 0–0 peak for CH8-4, CH8-4A, and CH8-4B gradually disappeared, demonstrating the molecular de-aggregation in the *o*-XY solutions. By analyzing the intensity ratio of $I_{0\text{-}0}/I_{0\text{-}1}$ between λ_{0-0} and λ_{0-1} at 25 °C (see the inset Figure in Figure 1c–1e), it can be concluded that the pre-aggregation effect was most pronounced for CH8-4A (0.127), subsequently followed by CH8-4 (0.106) and CH8-4B (0.075).

The pre-aggregation behaviors of CH8-4, CH8-4A, and CH8-4B can influence molecular packing behavior and crystallinity. Consequently, we performed the grazing incident wide-angle X-ray scattering (GIWAXS) measurements for their neat films. As shown in Figure 1f–1h, all neat films displayed a clear (100) diffraction peak in the in-plane (IP) direction and a strong (010) diffraction peak in the out-of-plane (OOP) direction, suggesting their favorable face-on orientation of the molecular packing.[34,35] By analyzing their line-cut profiles (Figure S4), we also identified (010) π–π stacking diffraction peaks at q_z values of 1.63, 1.65, and 1.64 $Å^{-1}$, corresponding to π–π distances of 3.85, 3.81, and 3.84 Å for CH8-4, CH8-4A, and CH8-4B neat films, respectively. The CH8-4, CH8-4A, and CH8-4B samples exhibited similar lamellar stacking (100) peaks in the IP direction at 0.27, 0.27, and 0.28 $Å^{-1}$, respectively. Notably, the coherence lengths (CL) for the (010) in OOP and (100) in IP directions of CH8-4, CH8-4A, and CH8-4B followed a consistent trend (Tables S2). In detail, the CL value for CH8-4 was 16.7 Å in the OOP direction and 50.0 Å in the IP direction, which were lower than those of CH8-4A (17.0 Å in OOP and 56.0 Å in IP) and higher than those of CH8-4B (16.0 Å in OOP and 47.1 Å in IP). These findings suggest the CH8-4A exhibits the most compact molecular stacking and molecular crystallinity of CH8-4A, echoing its most pronounced pre-aggregation motifs. Among them, the moderate molecular crystallinity behavior of CH8-4 may be beneficial for realizing morphologic features with bi-contin-

uous D–A network and suitable D/A phase separation in the blend active layers.[36,37]

All CH8-4/4A/4B neat films exhibited similar and broad absorption spectra in the range of 600–900 nm, providing complementary absorption characteristics to those of the PM6 film (Figure S3b and S3d). Herein, their photovoltaic performances were assessed by fabricating conventional OSCs with the architecture of ITO/3-BPIC-F/PM6:Acceptors/PNDIT-F3N/Ag (Figure S5), where our recently developed self-assembled monolayer 3-BPIC-F served as the electron transporting layer,[38] and *o*-XY was utilized as the primary solvent. Following systematic optimization of the device fabrication processes (Tables S3–S9), satisfactory PCEs with FFs of approximately 75 % were achieved for *o*-XY processed OSCs with PM6:CH8-4/4A/4B active layers. Notably, the PM6:CH8-4 based binary device obtained a PCE of 18.1 % with a J_{sc} of 26.68 mA cm^{-2}, surpassing our previously reported results,[26] attributed to the usage of 3-BPIC-F and the hot-cast strategy.[38] Among them, the PM6:CH8-4A based device exhibited the highest V_{oc} of 0.920 V; however, it demonstrated the worst PCE of 16.7 %, with a J_{sc} of only 24.20 mA cm^{-2}, possibly due to the undesired morphologies caused by the excessive pre-aggregation of CH8-4A. For the CH8-4B, a satisfactory PCE of 17.8 % was attained, accompanied by a V_{oc} of 0.906 V and a high J_{sc} of 26.09 mA cm^{-2}. The current density-voltage (*J–V*) characteristics of the optimized PM6:CH8-4/4A/4B devices are presented in Figure 2a, with the corresponding photovoltaic parameters summarized in Table 1. Obviously, compared to those with CH8-4A and CH8-4B, the higher PCE of the CH8-4-based device can be attributed to its significantly enhanced J_{sc}, which could be correlated with its improved charge generation and transport dynamics, as discussed below. Based on the PM6:CH8-4 host binary blend, we subsequently incorporated L8-BO-D (with its chemical structure depicted in Figure S6) as the third component to construct ternary OSCs, which exhibited no pre-aggregation effect in *o*-XY (Figure S7). This strategy further enhanced the V_{oc}, J_{sc} and FF, achieving an excellent PCE of 20.0 %, with a V_{oc} of 0.906 V, J_{sc} of 27.70 mA cm^{-2}, and FF of 79.6 %. To our knowledge, this state-of-the-art efficiency, approaching 20 %, represents an advancement of dimeric acceptor-based OSCs, narrowing the efficiency gap with small-molecular acceptors based OSCs.[39]

To validate the accuracy of the *J–V* measurement, we analyzed the EQE spectra of the PM6:CH8-4/4A/4B devices

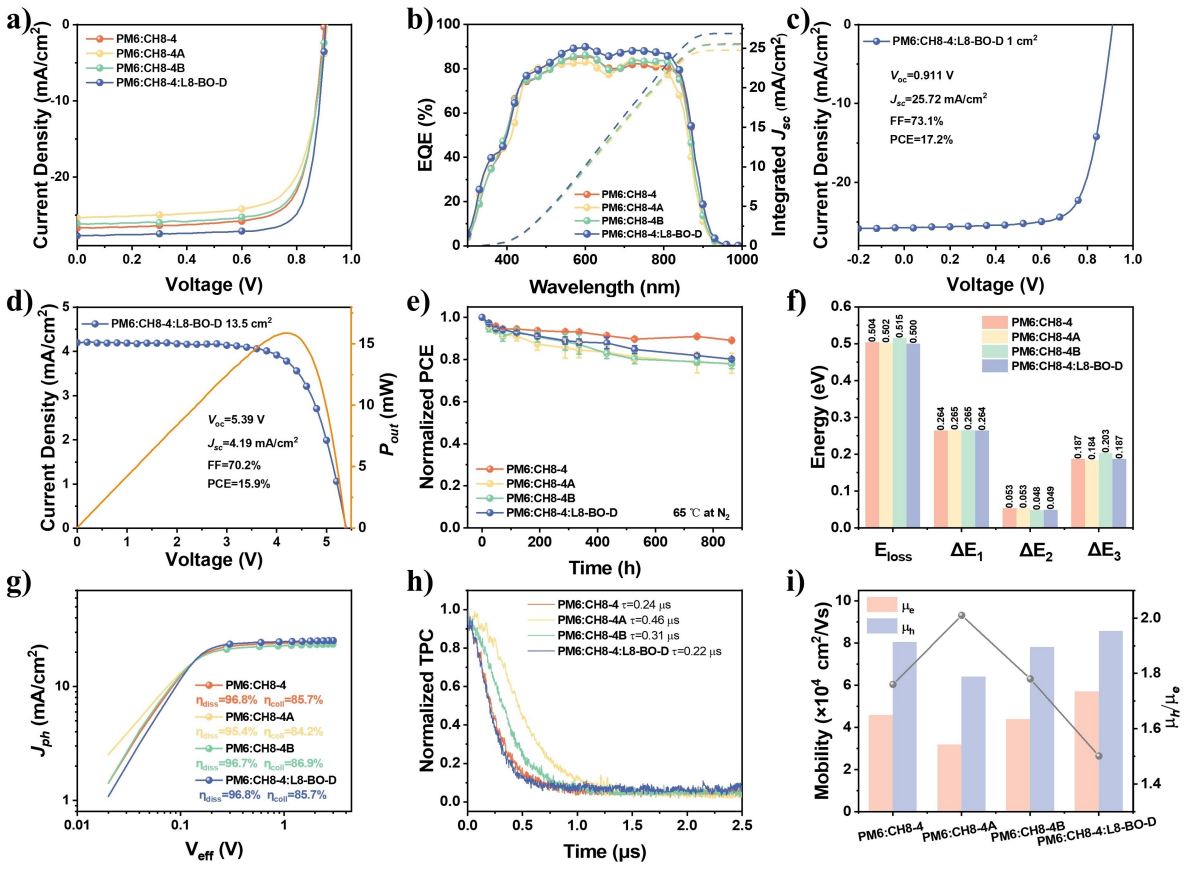

Figure 2. (a) *J–V* curves of the PM6:CH8-4/4A/4B and PM6:CH8-4:L8-BO-D OSCs. (b) EQE and corresponding integrated J_{sc} spectra of the PM6:CH8-4/4A/4B and PM6:CH8-4:L8-BO-D OSCs. (c) *J–V* curves of the best device based on 1 cm^2 devices. (d) *J–V* curves and output power density of 13.5 cm^2 modules via blade-coating. (e) Thermal stability of the devices. (f) Energy losses of PM6:CH8-4/4A/4B and PM6:CH8-4:L8-BO-D. (g) J_{ph} - V_{eff} curves. (h) Transient photocurrent characteristics and (i) Hole and electron mobilities of PM6:CH8-4/4A/4B and PM6:CH8-4:L8-BO-D based optimal devices.

Table 1: Photovoltaic performance parameters of best devices based on CH8-4/4A/4B binary devices and CH8-4 ternary devices, respectively.

BHJ	V_{oc} (V)	J_{sc} (mA cm^{-2})	$J_{sc,\,cal}$ (mA cm^{-2})	FF%	PCE[a]%
PM6 : CH8-4	0.901 (0.901 ± 0.002)	26.68 (26.55 ± 0.19)	25.53	75.4 (75.1 ± 0.2)	18.1 (18.0 ± 0.1)
PM6 : CH8-4A	0.920 (0.918 ± 0.002)	24.20 (24.30 ± 0.12)	23.05	74.5 (73.9 ± 0.4)	16.7 (16.5 ± 0.1)
PM6 : CH8-4B	0.906 (0.904 ± 0.002)	26.09 (26.13 ± 0.09)	25.46	75.2 (74.9 ± 0.2)	17.8 (17.7 ± 0.1)
PM6 : CH8-4 : L8-BO-D	0.906 (0.908 ± 0.001)	27.70 (27.46 ± 0.21)	26.87	79.6 (79.2 ± 0.6)	20.0 (19.8 ± 0.1)
PM6 : CH8-4 : L8-BO-D [b]	0.911	25.72	/	73.1	17.2
PM6 : CH8-4 : L8-BO-D [c]	5.392	4.20	/	70.2	15.9

[a] Average parameters were calculated based on 10 independent cells (Table S9). [b] 1 cm^2 device prepared by spin-coating method in glovebox; [c] 13.5 cm^2 module device consisting of 6 series-connected sub-cells prepared by blade-coating method in ambient.

(Figure 2b). The EQE spectra of all devices exhibited a broad spectral response in the range of 300–900 nm, consistent with the complementary absorption spectra of PM6 and the acceptors.[5] Notably, CH8-4 exhibited a slightly broader, red-shifted EQE response compared to CH8-4A and CH8-4B. Moreover, the EQEs of the PM6 : CH8-4 devices were much higher in the range of 650–820 nm corresponding to the CH8-4 contributions, indicating an efficient photoelectric conversion process, leading to the highest J_{sc} value of this device.[26] The calculated current densities ($J_{sc,\,CAL}$) derived from EQE curves are 25.53, 23.05, and 25.46 mA cm^{-2} for the PM6 : CH8-4/4A/4B devices, respectively, verifying the reliability of J_{sc}s obtained from *J*–*V* measurements. In addition, the incorporation of L8-BO-D to the host PM6 : CH8-4 binary blend led to an obvious enhancement of EQE response values from 500 nm to 850 nm, resulting in a 1.34 mA cm^{-2} enhancement in $J_{sc,\,CAL}$ for PM6 : CH8-4 : L8-BO-D ternary device. These results are also well-consistent with those extracted from the *J*–*V* curves, supporting the reliability of our results.

Based on the PM6 : CH8-4 : L8-BO-D ternary blend, a device with an effective area of 1 cm^2 and a module consisting of six sub-cells connected in series with an effective area of 13.5 cm^2 were successfully fabricated. The schematic diagram of the module was shown in Figure S8. Their *J*–*V* curves are presented in Figures 2c and 2d, with the corresponding photovoltaic parameters summarized in Table 1. As a result, the 1 cm^2 device yielded a PCE of 17.2 %, and the modules fabricated via blade-coating method exhibited an impressive PCE of 15.9 %. In addition, the modules fabricated via spin-coating method also exhibited an ideal PCE of 14.9 % (Table S6), indicating that the modules of the CH8-4 system can maintain consistent photovoltaic performance under different coating methods. This result demonstrating the potential of such acceptors in practical applications. Furthermore, we investigated the thermal stability, an important factor alongside PCE for practical applications, of the prepared 3D-NFA-based devices at a constant temperature of 65 °C under a nitrogen atmosphere (Figure 2e). All devices exhibited good thermal stability, with the PM6 : CH8-4 device retaining 89 % of its initial PCE after thermal aging for 870 h, compared to 80 % for the devices utilizing PM6 : CH8-4A/4B. Besides, the PCEs of PM6: CH8-4/4A/4B and PM6 : CH8-4 : L8-BO-D based devices maintained 61 %, 54 %, 57 % and 71 % of their original PCEs after 200 hours of light aging under maximum power point (MPP) tracking in a nitrogen-filled glovebox (Figure S9), respectively. By incorporating small molecular acceptor L8-BO-D into the blend, the ternary OSC still exhibits good thermal stability and improved photostability, providing vigorous support for facilitating their commercial applications.

To elucidate the V_{oc} variations of these 3D NFAs, we analyzed the energy loss (E_{loss}) in accordance with the principles of detailed balance theory.[40] The total E_{loss} was measured to be 0.504, 0.502, and 0.515 eV for PM6 : CH8-4/4A/4B based devices, respectively. The relevant data are summarized in Table S10. As shown in Figure 2f, the isomerism effect related to the F link site had only a minor influence on the recombination energy losses above the band gap (ΔE_1) for all optimized OSC devices, which are approximately 0.265 eV. The radiative recombination energy losses below the band gap (ΔE_2) decreased gradually from 0.053 eV in the CH8-4/4A devices to 0.048 eV in the CH8-4B devices. In view of the small difference of ΔE_1 and ΔE_2 in these devices, we conclude that change of E_{loss} in the binary device is mainly originated from ΔE_3.[41] The PM6 : CH8-4 and PM6 : CH8-4A devices demonstrated low non-radiative recombination energy loss of $\Delta E_3 = 0.187$ and 0.184 eV, where CH8-4B binary blend yielded the highest ΔE_3 of 0.203 eV among the binary devices, owing to its low EQE_{EL} values and increased energetic disorder (Figure S10).[42] The suppressed ΔE_3 played a crucial contribution to the smallest E_{loss} observed for the PM6 : CH8-4 device among the three NFAs, indicating a better trade-off between V_{oc} and J_{sc} to endow a relatively high J_{sc} of 26.68 mA/cm^2 and maximized PCE (18.1 %). Upon adding L8-BO-D into PM6 : CH8-4 blend, the CH8-4 ternary device showed an impressively low non-radiative energy loss (ΔE_3) of 0.187 eV, consequently exhibiting a reduced E_{loss} of 0.500 eV. Such a result indicates that the introduction of L8-BO-D can restrain energy loss, thus offering higher V_{oc} for the corresponding ternary device.

We comprehensively analyzed charge dissociation, transport, and recombination properties to further investigate the disparities in the J_{sc} values of the CH8-4/4A/4B devices. Figure 2g shows the relationship between photocurrent density (J_{ph}) and effective voltage (V_{eff}). The exciton dissociation efficiencies (η_{diss}) were determined by the ratio of J_{ph} under short-circuit conditions to the saturation current density (J_{sat}).[43] The PM6:CH8-4 and PM6:CH8-4B devices showed high η_{diss} about 0.968, whereas the PM6:CH8-4A device exhibited only 0.954. Additionally, the charge collection efficiency (η_{coll}) was calculated as the ratio of J_{ph} under maximum output condition to J_{sat}, which is 0.857 for the CH8-4 binary and ternary devices, higher than that of PM6:CH8-4A (0.842) but lower than PM6:CH8-4B (0.869). Although CH8-4B exhibited the best η_{diss} and η_{coll} values, the J_{sc} of PM6:CH8-4B was undesirable due to its blue-shifted optical absorption and increased non-radiative recombination. With the incorporation of L8-BO-D, the CH8-4 ternary device maintains the same exciton dissociation and charge collection efficiencies as CH8-4 binary blend. The efficient exciton generation and charge collection at D/A interface ensures satisfactory J_{sc} for both CH8-4 binary and ternary devices.[8] Furthermore, the charge recombination kinetics of the PM6:CH8-4/4B and PM6:CH8-4:L8-BO-D devices were revealed by measuring J_{sc} under different light intensities (P). This relationship was expressed as J_{sc}/P^{S}.[44] As displayed in Figure S11a and Table S11, the resultant S values for all devices ranged from 0.98–1.00, suggesting similar low bimolecular recombination. Additionally, a comparative analysis was conducted by plotting the V_{oc} against P, normalized by a factor of "nkT/qP_{in}". Figure S11b shows the slope obtained for the PM6:CH8-4 device (1.10 kT/q) was lower than those of the PM6:CH8-4A (1.19 kT/q) and CH8-4B (1.13 kT/q) devices, demonstrating effective suppression of trap-assisted recombination in PM6:CH8-4.[45] The calculated slope for PM6:CH8-4:L8-BO-D devices is 1.04 kT/q, demonstrating the incorporation of L8-BO-D further suppresses the trap-assisted recombination.[41]

We further investigated the OSC charge dynamic properties by measuring the transient photocurrent (TPC) and transient photovoltage (TPV).[31,46] The CH8-4 binary device exhibited the shortest charge extraction time of 0.24 μs (Figure 2h), outperforming both PM6:CH8-4A (0.46 μs) and PM6:CH8-4B (0.31 μs), indicating the most efficient charge extraction with minimal charge trapping. Furthermore, the photo-generated carrier lifetime of the CH8-4 binary device (17.38 μs) derived from the TPV profile (Figure S12) was longer than that of PM6:CH8-4A (5.24 μs) and PM6:CH8-4B (15.04 μs), indicating suppressed charge carrier recombination. Subsequently, in order to study the charge transport abilities, hole- and electron-only devices were fabricated to estimate the charge carrier mobility using the space charge - limited current (SCLC) method (Figure S13).[47] As presented in Figure 2i and Table S12, the corresponding μ_h/μ_e ratios of PM6:CH8-4/4A/4B blend films were found to be 1.76, 2.01, and 1.78, respectively. The PM6:CH8-4 device exhibited balanced hole (8.04×10^{-4} cm^2/Vs) and electron (4.58×10^{-4} cm^2/Vs) mobilities, which contribute to efficient charge transport and improved J_{sc} in the resulting OSCs.[4,26] With the incorporation of L8-BO-D, the ternary blend yields a longer carrier lifetime (20.63 μs), a more efficient carrier extraction process (0.22 μs) and higher carrier mobilities with a μ_h of 8.57×10^{-4} cm^2/V s and a μ_e of 5.70×10^{-4} cm^2/V s, giving a μ_h/μ_e ratio of 1.50. Overall, the significantly reduced charge recombination dynamics and the more balanced charge transport achieved in the ternary blend can partially explain the enhanced J_{sc} and FF. In addition, as shown in Figure S14 and Table S13, the electron mobilities of CH8-4/4A/4B in the neat films, measured by the space-charge limited current (SCLC) method are 5.89, 6.17 and 5.55×10^{-4} $cm^2V^{-1}s^{-1}$, respectively, suggesting their satisfactory charge transport ability.

The photovoltaic performances and charge dynamic properties of the CH8-4/4A/4B devices were partially determined by the morphologies of the blended films, which were probed by atomic force microscopy (AFM). As shown in Figure S15, all films exhibited smooth surfaces and successive phase separations with small root mean square (RMS) roughness values in the range of 1.16–1.25 nm, which benefited the establishment of efficient ohmic contacts with the electron transport layer (PNDIT-F3N). The distinct morphologies with consecutive nanofiber networks in the blended films, as compared to the neat films (Figure S16), are expected to be a key feature aiding efficient charge transportation and extraction process. We further employed AFM-based infrared (AFM-IR) spectroscopy to examine the fibril structures. The AFM-IR images revealed the distributions of the donor (PM6) and acceptor, as well as the fiber morphology, by analyzing the infrared absorption peak at 2216 cm^{-1} which unique to the cyano (C≡N) group in the acceptors (Figure 3a, blue and red colors represent PM6 and acceptor, respectively). The PM6:CH8-4/4B blends exhibited a typical co-continuous interpenetrating network, facilitating exciton dissociation and charge transport. In the CH8-4A binary film, the polymer donor was dispersed into very small domains and surrounded by the acceptor domains due to excessive pre-aggregation and crystallinity. This resulted in a lack of sufficient donor/acceptor interfaces and continuous channels for efficient charge transport, leading to an inferior J_{sc}. Additionally, the fibril diameters of AFM-IR images were estimated by the line-cut profiles in Figure S17, where the full-width at half-maximum of the peaks was used to estimate the fibril diameter.[48] As shown in Figure 3b, the average fibril diameters of PM6:CH8-4/4A/4B were 13.9, 15.1, and 13.1 nm, respectively. The moderate fibril diameters of the CH8-4 blended films can be ascribed to the improved crystallinity, which was consistent with GIWAXS results of the blend films (Figure S18–S19 and Table S14). Notably, with the incorporation of L8-BO-D into PM6:CH8-4 blend, the average fibril diameter of PM6:CH8-4:L8-BO-D decreased to 12.6 nm. Thus, a better morphology with appropriate domain size and well-defined fibrillar network is achieved in the ternary blend. The favorable morphology mediation induced by L8-BO-D may be attributed to its good non-halogenated solvent processability and superior miscibility with host acceptor of CH8-4.

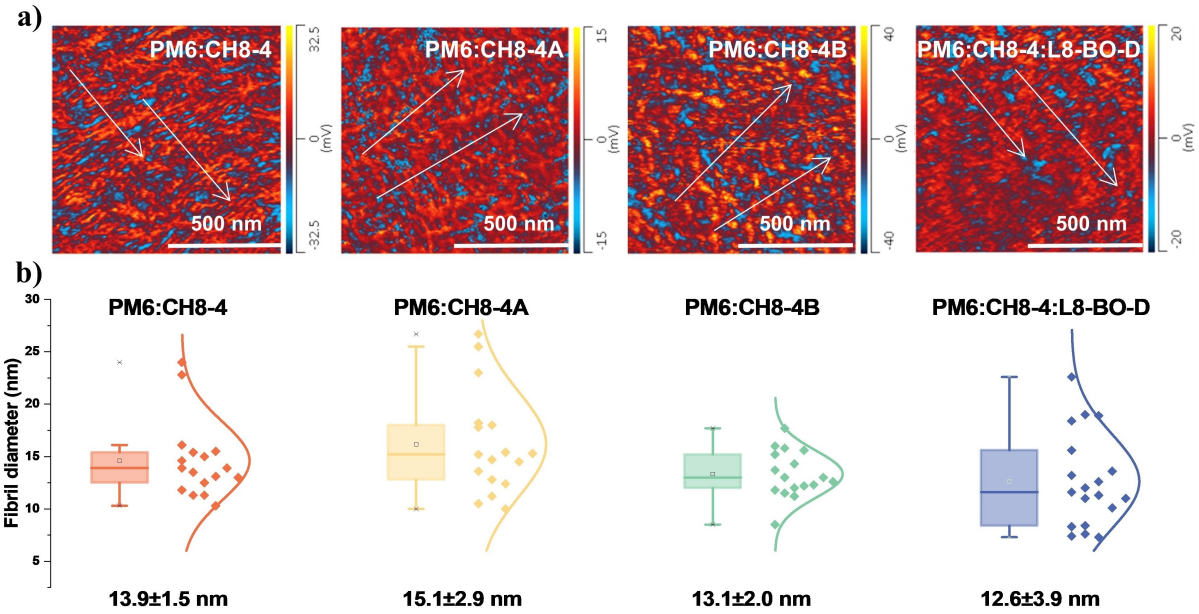

Figure 3. (a) Tapping AFM-IR image at the wavenumber of 2216 cm^{-1}, and (b) Statistical particle size distribution diagrams of PM6:CH8-4/4A/4B and PM6:CH8-4:L8-BO-D, respectively.

Additionally, the miscibility of the PM6 with the acceptors directly affects the fibril diameters and phase separation behavior. Therefore, we conducted the contact angle tests to calculate the surface energy and the Flory-Huggins interaction parameter (χ) (Figure S20–S21). The χ for blend to show the binary miscibility from $K(\sqrt{\gamma_D}-\sqrt{\gamma_A})^2$, where γ is the surface free energy of the material and $K=116\times10^3\ m^{1/2}$ is the proportionality constant. As evaluated in Table S15, CH8-4/4A/4B exhibited low χ values with PM6 of 0.18, 0.24, and 0.16 K, respectively. This implies good miscibility between PM6 and CH8-4/4A/4B, which is beneficial for supplying sufficient donor-acceptor interfaces for exciton dissociation.[13] Additionally, different morphology and fibril diameters of these 3D-NFAs blends play a decisive role in charge generation at D/A interfaces, which can be analyzed by the photoluminescence (PL) spectrum and PL quenching efficiency.[49] As illustrated in Figure S22 and Table S16, the PL quenching of all blend films were extremely high for PM6 (96.9–97.8 %), indicating that the charge generation were very efficient from PM6 to acceptors. Additionally, the PL quenching efficiency of the PM6:CH8-4/4A/4B compared to CH8-4, CH8-4A and CH8-4B neat films were 92.0 %, 87.1 %, and 96.3 %, respectively. With the incorporation of L8-BO-D, the PL quenching efficiency of CH8-4 ternary devices increased to 93.7 %, which is well consistent with the AFM-IR and fibril diameters results. The high PL quenching efficiency implied that excitons are rapidly dissociated into free carries at D/A interfaces in PM6:CH8-4/4B and PM6:CH8-4:L8-BO-D blends.

To analyze the film evolution kinetics during thermal annealing, the in situ thermal annealing absorptions of PM6:CH8-4/4A/4B and PM6:CH8-4:L8-BO-D blend films are depicted in Figure 4a, respectively. The absorption peak position of PM6 was barely changed during thermal annealing due to its high molecular weight and the tangled chains.[50] While there is an obvious red-shift in the locations of acceptors absorption peak, indicating that thermal annealing post-treatment could influence molecular aggregation and packing behaviors of these acceptors. The thermal annealing process of blend films could be divided into three stages: (I) heat conduction and residual solvent evaporation; (II) molecular rearrangement and (III) definitive morphology.[51] The maximum absorption peaks attributed to PM6 in all systems hardly change due to its high molecular weight and long chain structure, whereas there are obvious red-shifts in the maximum absorption peak positions of those acceptors. As depicted in Figure 4b, the following shifts in maximum absorption peaks were observed for PM6:CH8-4 blend (791 nm to 820 nm), the CH8-4A binary blend (775 nm to 814 nm), and PM6:CH8-4B blend (777 nm to 815 nm). The absorption peak positions in stage III align with those of the blend films (Figure S3c and S3d), signifying that molecular rearrangement and phase separation occurred during thermal annealing. The duration of the stage II for the PM6:CH8-4/4A/4B films was 0.5, 0.4, and 0.8 s, respectively, which is consistent with the different pre-aggregation abilities of those acceptors. These findings suggest that the different pre-aggregation abilities of these 3D dimeric acceptors can influence the rate of molecular rearrangement during thermal annealing. A long duration of the molecular rearrangement could allow sufficient time for the donor and acceptor to achieve improved phase separation and more uniform domains.[52,53] This result aligns with the AFM-IR findings. Additionally, the PM6:CH8-4:L8-BO ternary blend exhibited an extended molecular rearrangement time to 0.9 s compared to the CH8-4 binary device, indicating that the incorporation of L8-BO-D resulted in better phase separation and more uniform

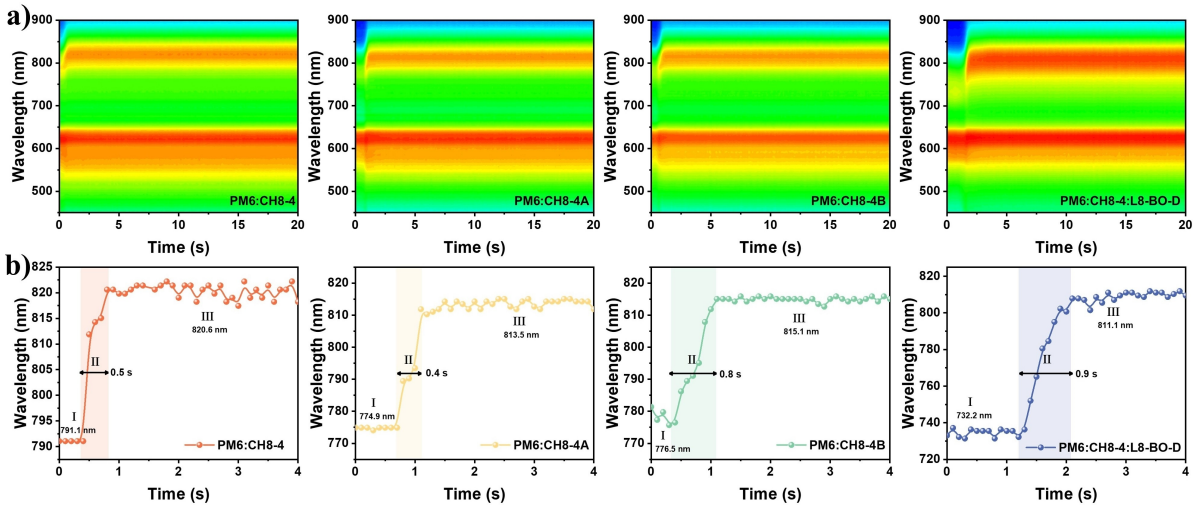

Figure 4. (a) In situ thermal annealing absorption spectra of the PM6:CH8-4/4A/4B and PM6:CH8-4:L8-BO-D films. (b) Dynamical evolution of the peak locations of CH8-4/4A/4B and CH8-4:L8-BO-D during thermal annealing, respectively.

morphology, which is beneficial for enhancing exciton dissociation and charge transport. Consequently, the ternary devices demonstrated improved V_{oc} and J_{sc} compared to binary devices. Notably, the onset time of redshift in the ternary system is delayed compared to the binary devices due to the excess amount of solid additive (2-MN) is incorporated in the ternary system. The sublimation of 2-MN is an endothermic process which results in slower evaporation of the residual solvent.[54]

The molecular dynamics (MD) simulations of PM6:CH8-4/4A/4B blends were conducted to investigate the effect of fluorine isomerism on intermolecular interactions (Figure 5a–c). As shown in Figure S23, PM6 was divided into two segments, labeled as C and E, while CH8-4/4A/4B acceptors were divided into four segments, labeled as F, A, D, and A′. Eight distinct packing conditions were identified. To illustrate the molecular packing scenarios, radial distribution functions (RDFs) between PM6 and these acceptors were calculated (Figure S24).[55] All blends demonstrated substantial increases in the range of 3.8–4.0 Å, which corresponded to the π–π packing distances determined through GIWAXS analysis. Among the eight stacking configurations, CH8-4 consistently exhibits favorable RDF peaks. Interestingly, under the CA packing conditions, the RDF shows a pronounced peak at the π–π stacking distances, indicating that the CH8-4 configuration contrib-

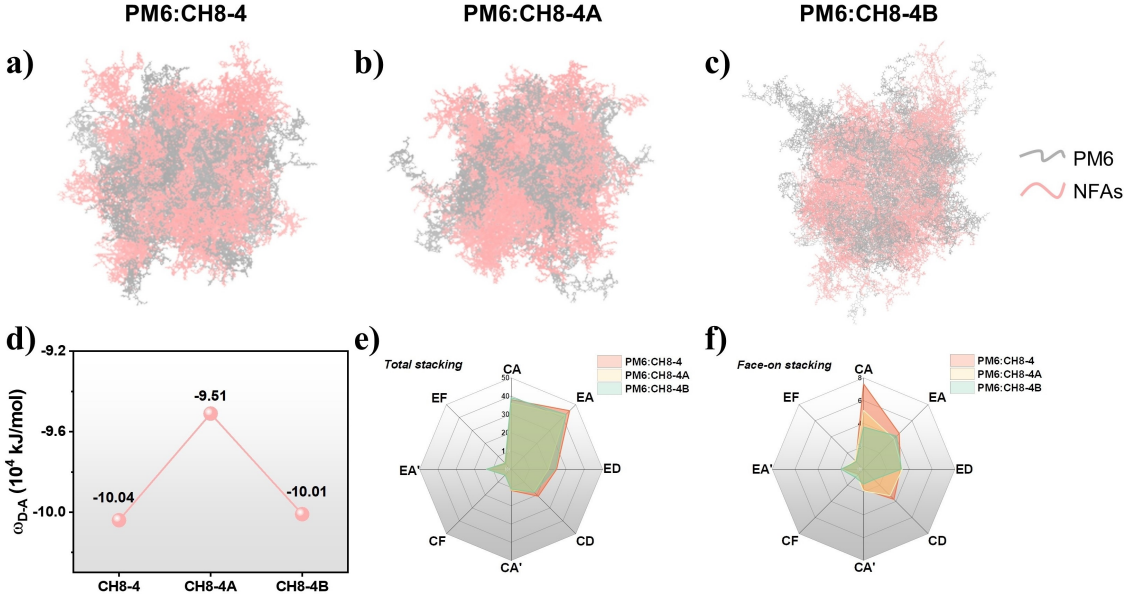

Figure 5. (a-c) MD simulation of the structure of PM6:CH8-4/4A/4B, where the pink and silver colors correspond to PM6 and CH8-4/4A/4B, respectively. (d) The interaction energies of PM6 and CH8-4/4A/4B. (e) Total stacking counts per unit volume comparison for PM6:CH8-4/4A/4B systems. (f) Face-on stacking counts per unit volume comparison for PM6:CH8-4/4A/4B systems.

utes to enhanced structural ordering within the system compared to other 3D acceptors. Meanwhile, the interaction energies (ω) of donor and acceptors were calculated to explore the reasons for the different molecular packing behaviors in PM6:CH8-4/4A/4B blends. As illustrated in Figure 5d, both electrostatic and van der Waals interactions (ω) between of PM6 to CH8-4 and CH8-4B were relatively stronger compared to CH8-4A, indicating enabling the formation of a tighter donor-acceptor interpenetrating network with better stacking.[56] These results align with the variation trend observed in the GIWAXS of blend films.

We characterized the dimer configurations arising from adjacent molecules to investigate the stacking mode in those binary systems. Specifically, we defined a dimer as a pair of molecules where the distance between the closest neighboring atoms is less than 5 Å. This characterization was based on two key parameters: the distance between the centers of mass (COM) of the molecular backbones (d), and the dihedral angle (φ) between the planes of the two molecules. The density heatmaps of d-φ can be found in Figure S25. An arrangement is classified as a face-on orientation when the dihedral angle φ is less than 30° and the COM distance d is less than 0.8 nm.[55] Typically, a face-on orientation promotes the most robust parallel π–π stacking interactions, resulting in enhanced electronic coupling, which is indicative of an improved charge transfer rate. Figure 5e-f show the total stacking and face-on stacking counts per unit volume for PM6:CH8-4/4A/4B systems, respectively. For total stacking, CH8-4 consistently shows a higher stacking counts across eight configurations compared to CH8-4A and 4B (Table S17). When considering face-on stacking, CH8-4 demonstrates the highest stacking counts, whereas CH8-4B shows the lowest (Table S18). The pronounced differences in stacking interactions between the CH8-4B system and the C segment of PM6 are primarily responsible for the observed variations. In the CH8-4B system, while the overall stacking of CA, CD, CA', and CF configurations is comparable to CH8-4 and 4B, the face-on stacking of CA, CD, and CA' is notably lower, whereas CF exhibits enhanced stacking. This phenomenon may be attributed to the F atom in CH8-4B being positioned furthest from the thiophene segment, reducing the electrostatic influence of the F atom on thiophene and resulting in a more negatively charged thiophene. Meanwhile, the C segment of PM6 shows a more positive electrostatic potential, particularly in the carbonyl region, which is significantly positively charged. Consequently, the face-on stacking of CF increases significantly, reducing the stacking of CA, CD, and CA′, thus impacting the overall stacking behavior. Overall, CH8-4′s superior total and face-on stacking numbers contribute to the observed improvement in power conversion efficiency (PCE) in the devices. Although CH8-4B has poorer face-on stacking numbers compared to CH8-4A, it exhibits better total stacking than CH8-4A, resulting in more charge transfer pathways, which consequently leads to the second-highest PCE. In contrast, CH8-4A, due to its inferior total stacking, results in the lowest PCE among the series. Additionally, MD simulations were performed on the PM6:CH8-4:L8-BO-D ternary system (Figure S26) to explore the impact of L8-BO-D addition on system efficiency. Correspondingly, we calculated the RDFs and stacking counts between the donor and acceptor molecules of CH8-4 ternary system. Figure S27 shows the distribution of total and face-on stacking counts for CH8-4 and L8-BO-D in the ternary system, respectively. The total and face-on stacking counts for CH8-4 in the ternary system are slightly lower than in the binary system. Nonetheless, this decrease is likely an unavoidable outcome of the enhanced structural order within the PM6:CH8-4:L8-BO-D system. The addition of L8-BO-D decreases the stacking density and promotes structural order, consequently enhancing the power conversion efficiency (PCE) of the devices.[57]

Conclusions

In summary, we synthesized a series of 3D dimeric NFAs (CH8-4, CH8-4A, and CH8-4B) by accurately modulating the fluorine atom positions to investigate the impact of isomerism on the properties of dimeric acceptors. When blended with polymer donor PM6, *o*-XY-processed PM6:CH8-4 device achieves a superior PCE of 18.1 %, surpassing PM6:CH8-4A (16.7 %) and PM6:CH8-4B (17.8 %), while also exhibiting good thermal stability. The highest PCE of PM6:CH8-4 is attributed to its moderate pre-aggregation ability and well-balanced charge transport characteristics. By contrast, PM6:CH8-4A exhibits the lowest PCE due to the excessive pre-aggregation of CH8-4A. Furthermore, incorporating L8-BO-D into the PM6:CH8-4 blend improves the exciton dissociation, diffusion, collection, and film morphology, resulting in an excellent ternary device with a PCE of 20.0 %, V_{oc} of 0.906 V, J_{sc} of 27.70 mA/cm^2, and FF of 79.6 %. This PCE record of 20.0 % is one of the best performances of dimerized acceptors based ternary devices. On the basis of these results, non-halogenated solvent *o*-XY-processed large-area modules with an active area of 13.5 cm^2 obtained an encouraging PCE approaching 16 %. This work provides an effective approach to control the pre-aggregation behavior of 3D dimeric acceptors in non-halogenated solvents and highlights the importance of molecular isomerization strategy in the innovation of efficient 3D dimeric acceptors intended for non-halogenated solvent-processed OSCs.

Acknowledgements

The authors gratefully acknowledge the financial support from National Natural Science Foundation of China (52303237, 21935007, 52025033, and 22361132530), Ministry of Science and Technology of the People's Republic of China (2022YFB4200400, 2019YFA0705900, 2023YFE0210400), and the Fundamental Research Funds for the Central Universities, Nankai University (023-632343116).

Conflict of Interest

The authors declare no competing interests.

Data Availability Statement

The data that support the findings of this study are available from the corresponding author upon reasonable request.

Keywords: Dimeric acceptor · non-halogenated solvent · isomerism effect · organic solar cells

[1] P. Gopikrishna, H. Choi, D. H. Kim, D. Lee, J. H. Hwang, S. M. Jin, E. Lee, S. Cho, B. Kim, *Small* **2024**, *20*, 2401080.
[2] T. Huang, S. Geng, D. Wang, Y. Zhang, N. Weng, X. Li, Q. Liao, Z. Zhang, J. Lu, J. Zhang, *Adv. Funct. Mater.* **2024**, *34*, 2315825.
[3] S. Guan, Y. Li, C. Xu, N. Yin, C. Xu, C. Wang, M. Wang, Y. Xu, Q. Chen, D. Wang, L. Zuo, H. Chen, *Adv. Mater.* **2024**, *36*, 2400342.
[4] C. Zhang, J. Yuan, J. K. W. Ho, J. Song, H. Zhong, Y. Xiao, W. Liu, X. Lu, Y. Zou, S. K. So, *Adv. Funct. Mater.* **2021**, *31*, 2101627.
[5] J. Wu, G. Li, J. Fang, X. Guo, L. Zhu, B. Guo, Y. Wang, G. Zhang, L. Arunagiri, F. Liu, H. Yan, M. Zhang, Y. Li, *Nat. Commun.* **2020**, *11*, 4612.
[6] M. Ghasemi, H. Hu, Z. Peng, J. J. Rech, I. Angunawela, J. H. Carpenter, S. J. Stuard, A. Wadsworth, I. McCulloch, W. You, H. Ade, *Joule* **2019**, *3*, 1328–1348.
[7] W. Zhou, J. Liu, J. Xie, S. You, J. Deng, F. Yu, S. Y. Jeong, H. Y. Woo, F. Wu, L. Chen, *Angew. Chem. Int. Ed.* **2024**, e202415141.
[8] C. Zhang, J. Song, J. Xue, S. Wang, Z. Ge, Y. Man, W. Ma, Y. Sun, *Angew. Chem. Int. Ed.* **2023**, *62*, e202308595.
[9] B. Fan, H. Gao, L. Yu, R. Li, L. Wang, W. Zhong, Y. Wang, W. Jiang, H. Fu, T. Chen, B. Kan, S.-W. Tsang, A. K.-Y. Jen, *Angew. Chem. Int. Ed.* **2024**, e202418439.
[10] S.-Y. Shi, C. Yang, X. Xu, Z.-X. Liu, W. Duan, X.-X. Chen, Z. Lu, H. Zhou, Z.-P. Yu, C.-Z. Li, *Angew. Chem. Int. Ed.* **2024**, e202415994.
[11] Y. Ding, W. A. Memon, D. Zhang, Y. Zhu, S. Xiong, Z. Wang, J. Liu, H. Li, H. Lai, M. Shao, F. He, *Angew. Chem. Int. Ed.* **2024**, *63*, e202403139.
[12] F. Yi, M. Xiao, Y. Meng, H. Bai, W. Su, W. Gao, Z.-F. Yao, G. Qi, Z. Liang, C. Jin, L. Tang, R. Zhang, L. Yan, Y. Liu, W. Zhu, W. Ma, Q. Fan, *Angew. Chem. Int. Ed.* **2024**, *63*, e202319295.
[13] M. Haris, Z. Ullah, S. Lee, D. H. Ryu, S. U. Ryu, B. J. Kang, N. J. Jeon, B. J. Kim, T. Park, W. S. Shin, C. E. Song, *Adv. Energy Mater.* **2024**, 2401597.
[14] X. li, X. Wu, Y. Gong, S. Qin, H. He, Z. Chen, T. Liang, C. Wang, D. Deng, Z. Bi, W. Ma, L. Meng, Y. Li, *Angew. Chem. Int. Ed.* **2024**, e202416016.
[15] T. Jia, Y. Luo, Y. Hai, T. Lin, X. Qin, R. Ma, K. Fan, A. A. Sergeev, T. A. Dela Peña, Y. Li, M. Li, K. S. Wong, G. Li, J. Wu, S. Liu, F. Huang, *Energy Environ. Sci.* **2024**, *17*, 8593–8608.
[16] H. Xia, Y. Zhang, K. Liu, W. Deng, M. Zhu, H. Tan, P. W. K. Fong, H. Liu, X. Xia, M. Zhang, T. A. Dela Peña, R. Ma, M. Li, J. Wu, Y. Lang, J. Fu, W.-Y. Wong, X. Lu, W. Zhu, G. Li, *Energy Environ. Sci.* **2023**, *16*, 6078–6093.
[17] W. Gao, R. Ma, T. A. Dela Peña, C. Yan, H. Li, M. Li, J. Wu, P. Cheng, C. Zhong, Z. Wei, A. K. Y. Jen, G. Li, *Nat. Commun.* **2024**, *15*, 1946.
[18] H. Bai, R. Ma, W. Su, T. A. D. Peña, T. Li, L. Tang, J. Yang, B. Hu, Y. Wang, Z. Bi, Y. Su, Q. Wei, Q. Wu, Y. Duan, Y. Li, J. Wu, Z. Ding, X. Liao, Y. Huang, C. Gao, G. Lu, M. Li, W. Zhu, G. Li, Q. Fan, W. Ma, *Nano-Micro Lett.* **2023**, *15*, 241.
[19] R. Ma, H. Li, T. A. Dela Peña, H. Wang, C. Yan, P. Cheng, J. Wu, G. Li, *Natl. Sci. Rev.* **2024**, *11*, nwae384.
[20] Z. Luo, W. Wei, R. Ma, G. Ran, M. H. Jee, Z. Chen, Y. Li, W. Zhang, H. Y. Woo, C. Yang, *Adv. Mater.* **2024**, *36*, 2407517.
[21] W. Wei, C. e Zhang, Z. Chen, W. Chen, G. Ran, G. Pan, W. Zhang, P. Müller-Buschbaum, Z. Bo, C. Yang, Z. Luo, *Angew. Chem. Int. Ed.* **2024**, *63*, e202315625.
[22] C. Wang, X. Ma, Y.-f. Shen, D. Deng, H. Zhang, T. Wang, J. Zhang, J. Li, R. Wang, L. Zhang, Q. Cheng, Z. Zhang, H. Zhou, C. Tian, Z. Wei, *Joule* **2023**, *7*, 2386–2401.
[23] J. Song, C. Zhang, C. Li, J. Qiao, J. Yu, J. Gao, X. Wang, X. Hao, Z. Tang, G. Lu, R. Yang, H. Yan, Y. Sun, *Angew. Chem. Int. Ed.* **2024**, *63*, e202404297.
[24] W. Liu, J. Wen, H. Yu, X. Zhan, Y. Wang, L. Zhang, Y. Fan, Z. You, Y. Liu, *Angew. Chem. Int. Ed.* **2024**, e202413135.
[25] H. Chen, Z. Zhang, P. Wang, Y. Zhang, K. Ma, Y. Lin, T. Duan, T. He, Z. Ma, G. Long, C. Li, B. Kan, Z. Yao, X. Wan, Y. Chen, *Energy Environ. Sci.* **2023**, *16*, 1773–1782.
[26] H. Chen, B. Kan, P. Wang, W. Feng, L. Li, S. Zhang, T. Chen, Y. Yang, T. Duan, Z. Yao, C. Li, X. Wan, Y. Chen, *Angew. Chem. Int. Ed.* **2023**, *62*, e202307962.
[27] Y. Li, Z. Ge, L. Mei, H. Ma, Y. Chen, X. Wang, J. Yu, G. Lu, R. Yang, X.-K. Chen, S. Yin, Y. Sun, *Angew. Chem. Int. Ed.*, *63*, e202411044.
[28] H. Zhuo, X. Li, J. Zhang, S. Qin, J. Guo, R. Zhou, X. Jiang, X. Wu, Z. Chen, J. Li, L. Meng, Y. Li, *Angew. Chem. Int. Ed.* **2023**, *62*, e202303551.
[29] H. Hu, S. Liu, J. Xu, R. Ma, Z. Peng, T. A. D. Peña, Y. Cui, W. Liang, X. Zhou, S. Luo, H. Yu, M. Li, J. Wu, S. Chen, G. Li, Y. Chen, *Angew. Chem. Int. Ed.* **2024**, *63*, e202400086.
[30] Z. Luo, W. Wei, R. Ma, G. Ran, M. H. Jee, Z. Chen, Y. Li, W. Zhang, H. Y. Woo, C. Yang, *Adv. Mater.* **2024**, *36*, 2407517.
[31] Y. Bai, T. Chen, X. Ji, J. Wang, W. Zhao, S. Yuan, Y. Zhang, G. Long, Z. Zhang, X. Wan, B. Kan, Y. Chen, *Adv. Energy Mater.* **2024**, *14*, 2400938.
[32] F. Eller, C. R. McNeill, E. M. Herzig, *Adv. Energy Mater.* **2024**, *14*, 2304455.
[33] D. Zhu, X. Bao, Q. Zhu, C. Gu, M. Qiu, S. Wen, J. Wang, B. Shahid, R. Yang, *Energy Environ. Sci.* **2017**, *10*, 614–620.
[34] C. Chen, L. Wang, W. Xia, K. Qiu, C. Guo, Z. Gan, J. Zhou, Y. Sun, D. Liu, W. Li, T. Wang, *Nat. Commun.* **2024**, *15*, 6865.
[35] W. Feng, T. Chen, Y. Li, T. Duan, X. Jiang, C. Zhong, Y. Zhang, J. Yu, G. Lu, X. Wan, B. Kan, Y. Chen, *Angew. Chem. Int. Ed.* **2024**, *63*, e202316698.
[36] T. Duan, J. Wang, W. Shi, Y. Li, K. Tu, X. Bi, C. Zhong, J. Lv, K. Yang, Z. Xiao, B. Kan, Y. Zhao, *Angew. Chem. Int. Ed.* **2024**, *63*, e202407890.
[37] Y. Guo, J. Sun, T. Guo, Y. Liu, Z. Yao, *Angew. Chem. Int. Ed.* **2024**, *63*, e202319664.
[38] H. Liu, Y. Xin, Z. Suo, L. Yang, Y. Zou, X. Cao, Z. Hu, B. Kan, X. Wan, Y. Liu, Y. Chen, *J. Am. Chem. Soc.* **2024**, *146*, 14287–14296.
[39] J. Ge, L. Xie, R. Peng, B. Fanady, J. Huang, W. Song, T. Yan, W. Zhang, Z. Ge, *Angew. Chem. Int. Ed.* **2020**, *59*, 2808–2815.
[40] Y. Wang, D. Qian, Y. Cui, H. Zhang, J. Hou, K. Vandewal, T. Kirchartz, F. Gao, *Adv. Energy Mater.* **2018**, *8*, 1801352.
[41] J. Ren, S. Zhang, Z. Chen, T. Zhang, J. Qiao, J. Wang, L. Ma, Y. Xiao, Z. Li, J. Wang, X. Hao, J. Hou, *Angew. Chem. Int. Ed.* **2024**, *63*, e202406153.

[42] J. Chantana, Y. Kawano, T. Nishimura, A. Mavlonov, T. Minemoto, *Sol. Energy Mater. Sol. Cells* **2020**, *210*, 110502.
[43] C. Yang, Q. An, M. Jiang, X. Ma, A. Mahmood, H. Zhang, X. Zhao, H.-F. Zhi, M. H. Jee, H. Y. Woo, X. Liao, D. Deng, Z. Wei, J.-L. Wang, *Angew. Chem. Int. Ed.* **2023**, *62*, e202313016.
[44] Z. Yao, X. Cao, X. Bi, T. He, Y. Li, X. Jia, H. Liang, Y. Guo, G. Long, B. Kan, C. Li, X. Wan, Y. Chen, *Angew. Chem. Int. Ed.* **2023**, *62*, e202312630.
[45] S. Zeiske, O. J. Sandberg, N. Zarrabi, W. Li, P. Meredith, A. Armin, *Nat. Commun.* **2021**, *12*, 3603.
[46] T. Duan, J. Wang, X. Zuo, X. Bi, C. Zhong, Y. Li, Y. Long, K. Tu, W. Zhang, K. Yang, H. Zhou, X. Wan, Y. Zhao, B. Kan, Y. Chen, *Mater. Horiz.* **2024**, *11*, 4413–4423.
[47] X. Zhao, Q. An, H. Zhang, C. Yang, A. Mahmood, M. Jiang, M. H. Jee, B. Fu, S. Tian, H. Y. Woo, Y. Wang, J.-L. Wang, *Angew. Chem. Int. Ed.* **2023**, *62*, e202216340.
[48] L. Zhu, M. Zhang, J. Xu, C. Li, J. Yan, G. Zhou, W. Zhong, T. Hao, J. Song, X. Xue, Z. Zhou, R. Zeng, H. Zhu, C. C. Chen, R. C. I. MacKenzie, Y. Zou, J. Nelson, Y. Zhang, Y. Sun, F. Liu, *Nat. Mater.* **2022**, *21*, 656–663.
[49] L. Zuo, S. B. Jo, Y. Li, Y. Meng, R. J. Stoddard, Y. Liu, F. Lin, X. Shi, F. Liu, H. W. Hillhouse, D. S. Ginger, H. Chen, A. K. Y. Jen, *Nat. Nanotechnol.* **2022**, *17*, 53–60.
[50] D. Qiu, C. Tian, H. Zhang, J. Zhang, Z. Wei, K. Lu, *Adv. Mater.* **2024**, *36*, 2313251.
[51] H. Chen, W. Sun, R. Zhang, Y. Huang, B. Zhang, G. Zeng, J. Ding, W. Chen, F. Gao, Y. Li, Y. Li, *Adv. Mater.* **2024**, *36*, 2402350.
[52] Z. Liu, Y. Fu, J. Wu, X. Yi, M. Zhao, M. Huang, J. Liu, Z. Xie, *Adv. Funct. Mater.* **2024**, 2401558.
[53] Y. Xiao, H. Yao, J. Wang, T. Zhang, Z. Chen, J. Qiao, N. Yang, Y. Yu, J. Ren, Z. Li, X. Hao, J. Hou, *Adv. Energy Mater.* **2024**, *14*, 2400928.
[54] J. Song, Y. Li, Y. Cai, R. Zhang, S. Wang, J. Xin, L. Han, D. Wei, W. Ma, F. Gao, Y. Sun, *Matter* **2022**, *5*, 4047–4059.
[55] J. Wang, T. Chen, W. Zhao, X. Tang, Y. Bai, W. Zhou, G. Long, X. Ji, G. Lu, W. Feng, X. Wan, B. Kan, Y. Chen, *Adv. Funct. Mater.* **2024**, *12*, 2414941.
[56] T. Hu, X. Zheng, C. Xiao, J. Su, A. Saparbaev, M. Wan, J. Wu, H. Xiang, Y. Yu, E. Wang, X. Wang, R. Yang, *Nano Energy* **2024**, *130*, 110172.
[57] C. Liu, N. Qiu, H. Liu, Y. Kan, Y. Sun, K. Gao, C. Li, Y. Lu, *Adv. Funct. Mater.* **2024**, 202414292.

Manuscript received: December 3, 2024
Accepted manuscript online: December 26, 2024
Version of record online: ■■, ■■

Research Article

Organic Solar Cells

J. Wang, P. Wang, T. Chen, W. Zhao, J. Wang, B. Lan, W. Feng, H. Liu, Y. Liu, X. Wan, G. Long, B. Kan,* Y. Chen* _____ **e202423562**

Isomerism Effect of 3D Dimeric Acceptors for Non-Halogenated Solvent-Processed Organic Solar Cells with 20% Efficiency

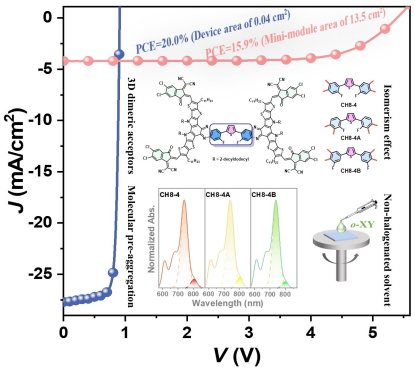

Molecular isomerization strategy was employed to develop 3D dimeric acceptors (CH8-4/4A/4B), which demonstrate varying molecular pre-aggregation in *o*-xylene. These distinctive properties significantly affect the film-forming process and the resulting morphological characteristics. Due to the moderate pre-aggregation of CH8-4, an impressive efficiency of 20.0% was received for CH8-4-based device, representing the state-of-the-art in non-halogen solvent-processed organic solar cells.